Journal of Alloys and Compounds 652 (2015) 470–478

Contents lists available at ScienceDirect

Journal of Alloys and Compounds

journal homepage: http://www.elsevier.com/locate/jalcom

Search for Fe magnetic ordering in the 40 K superconductor ($Li_{0.8}Fe_{0.2}$)OHFeSe

Farshad Nejadsattari, Zbigniew M. Stadnik*

Department of Physics, University of Ottawa, Ottawa, Ontario K1N 6N5, Canada

ARTICLE INFO

Article history:
Received 27 July 2015
Received in revised form
25 August 2015
Accepted 26 August 2015
Available online 31 August 2015

Keywords:
Superconductivity
^{57}Fe Mössbauer spectroscopy
Ferromagnetism
Antiferromagnetism
Debye temperature

ABSTRACT

We report the results of x-ray diffraction and ^{57}Fe Mössbauer spectroscopy study, complemented by *ab-initio* electronic structure and the hyperfine-interaction parameters calculations, of the 40 K superconductor ($Li_{0.8}Fe_{0.2}$)OHFeSe. The superconductor crystallizes in the tetragonal space group *P*4/*nmm* with the lattice constants $a = 3.7865(2)$ Å and $c = 9.2802(6)$ Å. Evidence is provided for the presence of an anisotropic mixture of strong covalent and weak ionic chemical bonding and of metallic characteristics. The Mössbauer spectra consist of two quadrupole-doublet patterns corresponding to Fe^{2+} at the 2*a* and 2*b* sites. Contrary to the claims in the literature, we demonstrate unequivocally that there is no magnetic ordering of the 2*a*-site Fe magnetic moments down to 2.0 K. The calculated hyperfine-interaction parameters at the two Fe sites show general agreement with the experimental ones. The Debye temperatures for the 2*a* and 2*b* sites are found to be 186(21) and 397(4) K, respectively.

1. Introduction

The tetragonal binary phase β-$Fe_{1.01}$ Se exhibits superconductivity below the critical temperature $T_c \approx 8.5$ K [1,2]. Intercalation of alkali metals, alkali earths, rare earths (A) or small molecules into the adjacent FeSe layers increases the T_c value of the derived superconductors A_xFe_{2-y} Se_2 [3,4], $Li_x(C_5H_5N)_yFe_{2-z}$ Se_2 [5], and $Li_x(NH_2)_y(NH_3)_{1-y}$ Fe_2 Se_2 (Ref. [6]) up to ~46 K. Films of FeSe one unit cell thick grown on $SrTiO_3$ substrates become superconducting [7–10] below ~65 K – the highest T_c in the Fe-based superconductors.

Very recently, new FeSe-derived superconductors ($Li_{0.8}$ $Fe_{0.2}$)OHFeSe (Refs. [11,12]) with $T_c \approx 40$ K, ($Li_{0.8}$ $Fe_{0.2}$)OH($Fe_{0.92}$ Li)0.08 Se (Ref. [13]) with $T_c = 43$ K, and the series (Li_{1-x} Fe_x)OHFeSe [14], (Li_{1-x} Fe_x)OHFe_{1-y} Se [15], and ($Li_{0.8}$ $Fe_{0.2}$)OHFe(S_{1-x} Se_x) (Ref. [16]) with T_c values up to 40 K, were discovered. What is particularly interesting about these new superconductors is the claim of the existence in them of long-range, 3*d* magnetic ordering with ordering temperatures much lower than T_c. In particular, canted antiferromagnetism at ~8.5 K (Ref. [11]) or field-induced ferromagnetism [12] were suggested to exist in the ($Li_{0.8}$ $Fe_{0.2}$)OHFeSe superconductor. In a superconductor of a similar composition, ($Li_{0.8}$ $Fe_{0.2}$)OH($Fe_{0.92}$ Li)0.08 Se, ferromagnetism with the Curie temperature $T_C \approx 10$ K was suggested [13]. In both superconductors, the magnetic ordering was suggested to be associated with Fe atoms located at a site in the hydroxide layer [11–13].

Whereas the coexistence of the commonly believed antagonistic phenomena of superconductivity and long-range, 3*d* magnetic order in the bulk is not impossible, it is nevertheless surprising. Since the putative magnetic order is associated with the Fe atoms, the best way to assess whether it is intrinsic to the superconducting phase, or is due to extrinsic effects (such as magnetic secondary phases or grain boundaries), is to use an Fe-sensitive local probe. Here we use the ^{57}Fe Mössbauer spectroscopy [17] to demonstrate unequivocally that the Fe magnetic moments in the 40 K superconductor ($Li_{0.8}$ $Fe_{0.2}$)OHFeSe do not order magnetically down to 2.0 K.

2. Experimental and theoretical methods

The polycrystalline sample of composition ($Li_{0.8}$ $Fe_{0.2}$)OHFeSe was prepared by the hydrothermal reaction method, as described earlier [11].

An X-ray diffraction measurement was carried out at 298 K in Bragg-Brentano geometry on a PANalytical X'Pert scanning diffractometer using Cu $K\alpha$ radiation in the 2θ range 5–80° in steps of 0.02°. The $K\beta$ line was eliminated by using a Kevex PSi2 Peltier-cooled solid-state Si detector.

* Corresponding author.
E-mail address: stadnik@uottawa.ca (Z.M. Stadnik).

http://dx.doi.org/10.1016/j.jallcom.2015.08.216
0925-8388/

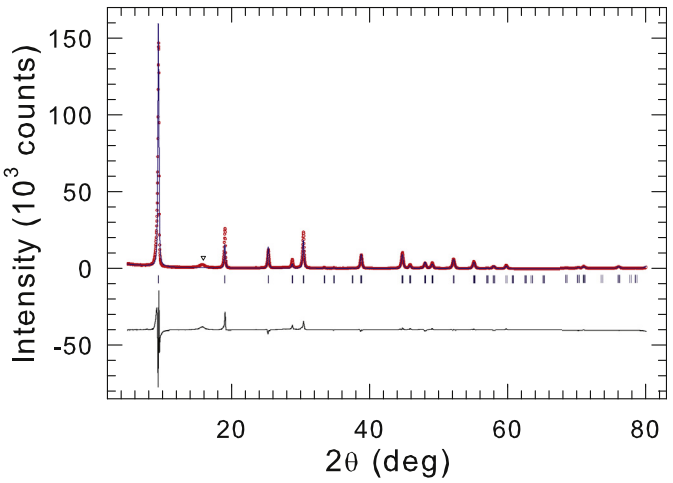

Fig. 1. Powder x-ray diffraction pattern of ($Li_{0.8}Fe_{0.2}$)OHFeSe at 298 K. The experimental data are denoted by open circles, while the line through the circles represents the results of the Rietveld refinement. The row of vertical bars shows the Bragg peak positions for the *P*4/*nmm* space group. The lower solid line represents the difference curve between experimental and calculated patterns. The symbol ▽ indicates the Bragg peak position of an unidentified impurity phase.

The ^{57}Fe Mössbauer measurements were conducted using a standard Mössbauer spectrometer operating in sine mode and a ^{57}Co(Rh) source at room temperature. The spectrometer was calibrated with a 6.35-μm-thick α-Fe foil [18] and the spectra were folded. The Mössbauer absorber was made in a glove box. The powder material was mixed with boron nitride and was put into a high-purity, 8-μm-thick Al disk container to ensure a uniform temperature over the whole absorber. The Mössbauer absorber was exposed to air for about 50 s when it was transported from the glove box to the Mössbauer cryostat in which it was kept in a static exchange gas atmosphere at the pressure of ~5×10^{-3} mbar. The surface density of the prepared Mössbauer absorber of 17.3 mg/cm^2 corresponds to an effective thickness parameter [17] $t_a = 4.0 f_a$, where f_a is the Debye-Waller factor of the absorber. Since $t_a > 1$, the resonance line shape of the Mössbauer spectrum was described using a transmission integral formula [19]. The source linewidth of 0.12 mm/s and the background-corrected Debye-Waller factor of the source of 0.60 were used in the fits of the Mössbauer spectra [19].

Ab initio electronic structure and Mössbauer hyperfine-interaction parameter calculations have been performed within the framework of density functional theory using the full-potential linearized augmented-plane-wave plus local orbitals (FP-LAPW+ lo) method, as implemented in the WIEN2k package [20]. In this method, one partitions the unit cell into two regions: a region of non-overlapping muffin-tin (MT) spheres centered at the atomic sites and an interstitial region. The wave functions in the MT regions are a linear combination of atomic radial functions times spherical harmonics, whereas in the interstitial regions they are expanded in plane waves.

Table 1
Atomic positions for the tetragonal ($Li_{0.8}$ $Fe_{0.2}$)OHFeSe (space group *P*4/*nmm*, origin choice 2) obtained through Rietveld analysis.

Atom	Site	Point symmetry	Occupancy	*x*	*y*	*z*
Li	2*a*	$\bar{4}$ m2	0.82(1)	$\frac{3}{4}$	$\frac{1}{4}$	0
Fe_1	2*a*	$\bar{4}$ m2	0.18(1)	$\frac{3}{4}$	$\frac{1}{4}$	0
O	2*c*	4 *mm*	1.0	$\frac{1}{4}$	$\frac{1}{4}$	−0.074(2)
H	2*c*	4 *mm*	1.0	$\frac{1}{4}$	$\frac{1}{4}$	0.174(2)
Fe_2	2*b*	$\bar{4}$ m2	1.00	$\frac{3}{4}$	$\frac{1}{4}$	$\frac{1}{2}$
Se	2*c*	4 *mm*	1.0	$\frac{1}{4}$	$\frac{1}{4}$	0.338(2)

The basis set inside each MT sphere is split into a core and a valence subset. The core states are treated within the spherical part of the potential only and are assumed to have a spherically symmetric charge density in the MT spheres. The valence wave functions in the interstitial region were expanded in spherical harmonics up to $l = 4$, whereas in the MT region they were expanded to a maximum of $l = 12$ harmonics. For the exchange-correlation potential, the generalized gradient approximation (GGA) scheme of Perdew, Burke, and Ernzerhof [21] was used. A separation energy of −6.0 Ry between the valence and core states of individual atoms in the unit cell was chosen. The initialization of the calculations was done using a $2a \times 2b \times c$ supercell in order to account for the fractional occupation of the 2*a* sites by the Li and Fe atoms.

The values of 0.59 a.u., 1.09 a.u., 2.30 a.u., 1.69 a.u., and 2.19 a.u. were used as the MT radii for H, O, Fe, Li, and Se, respectively. The plane-wave cut-off parameter was set to $R_{MT} \times K_{MAX} = 3$, where R_{MT} is the smallest MT radius in the unit cell and K_{MAX} is the maximum *K* vector used in the plane-wave expansion in the interstitial region. A total number of 100 *k*-points was used within a $10 \times 10 \times 10$ *k*-mesh in the first Brillouin zone. A convergence

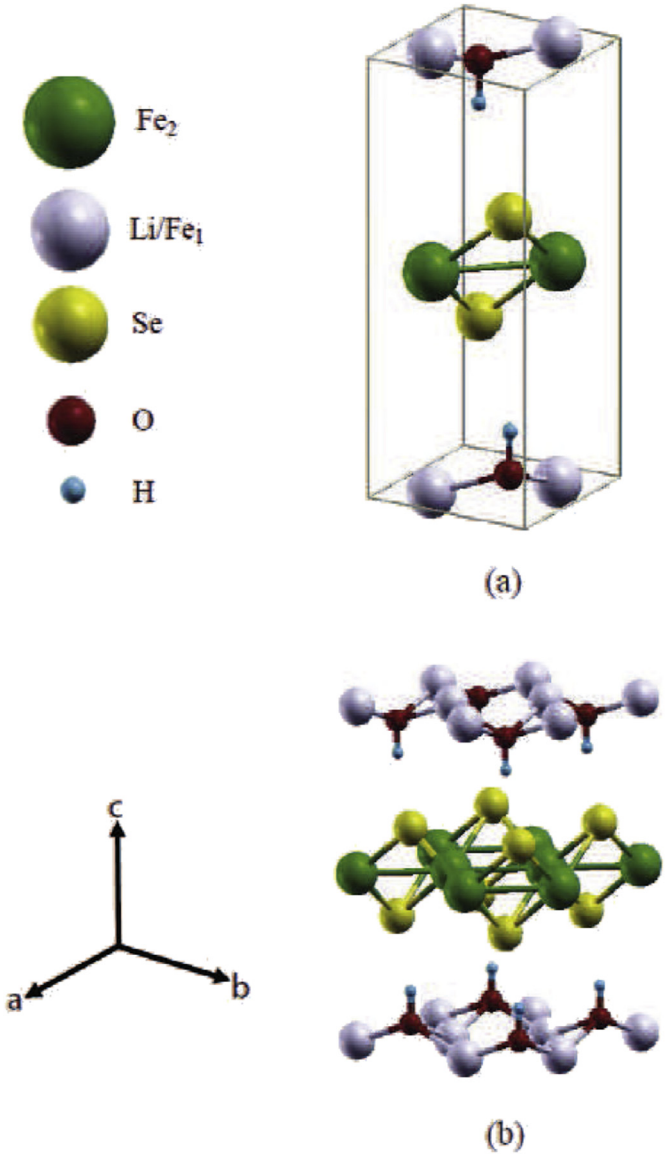

Fig. 2. The unit cell (a) and the layered crystal structure (b) of ($Li_{0.8}$ $Fe_{0.2}$)OHFeSe.

criterion for self-consistent field calculations was chosen in such a way that the difference in energy between two successive iterations did not exceed 10^{-4} Ry. The experimental lattice constants a and c and the atomic position parameters in the space group $P4/nmm$ (*vide infra*) were used in the calculations.

3. Results and discussion

3.1. Structural characterization

The room-temperature powder x-ray diffraction pattern of $(Li_{0.8}Fe_{0.2})$OHFeSe is shown in Fig. 1. The studied compound crystallizes in the tetragonal space group $P4/nmm$ (No. 129) [11]. A Rietveld refinement [22] of the pattern in Fig. 1 yields the lattice parameters $a = 3.7865(2)$ Å, $c = 9.2802(6)$ Å, and the atomic positional parameters that are listed in Table 1. The values of these parameters compare well with the corresponding values reported earlier [11,13]. We note that the Bragg peak at $2\theta \approx 15.9^{\circ}$ (Fig. 1) must originate from a small amount of an unidentified second phase present in the sample studied.

The crystal structure of $(Li_{0.8}Fe_{0.2})$OHFeSe in the $P4/nmm$ space group is shown in Fig. 2. The presence of covalent bonding (*vide infra*) is indicated pictorially by rods in the unit cell (Fig. 2).

3.2. Ab-initio calculations

3.2.1. Charge density distribution

The calculated valence charge density distribution in the (100), (001), and (110) planes is shown in Fig. 3. One notices that in the (100) plane [Fig. 3(a)], the charge density is concentrated along three structural layers. A strong covalent bonding between Fe, O, and H is observed for the top and bottom layers (green regions). A

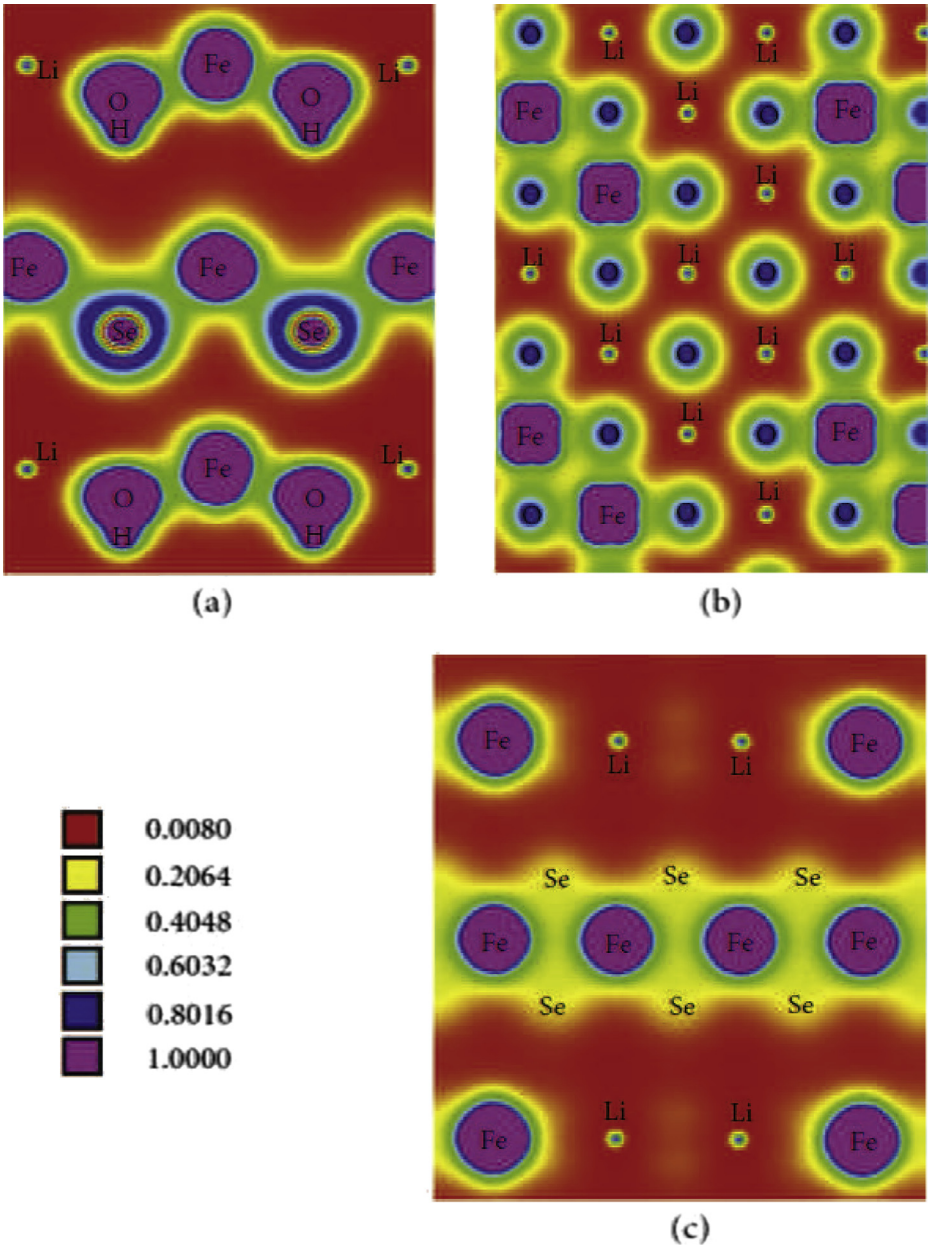

Fig. 3. Electron charge density distribution (in units of e/Å^3) in the (100) (a), (001) (b), and (110) (c) planes.

similar strong bonding between Fe and Se can be seen for the middle layer. However, the negligible charge density between the layers (red regions) indicates ionic bonding between them.

Fig. 3(b) shows that strong covalent bonds are formed between Fe and four neighboring O atoms. However, there is a negligible charge density in the vicinity of Li atoms which suggests that these atoms participate in ionic bonding. Weaker covalent bonds are formed between neighboring Fe atoms, and Fe and Se atoms, in the (110) plane [Fig. 3(c)].

By examining the valence charge densities in these three planes one can conclude that a relatively good electrical transport of this compound arises from Fe states forming strong covalent bonds. The directional covalent bonds between the atoms are also shown schematically by rods in the unit cell and the layered crystal structure of ($Li_{0.8}$ $Fe_{0.2}$)OHFeSe in Fig. 2. It is thus suggested that a relatively good electrical conductivity originates partially from the Fe–Se layers.

3.2.2. Electronic structure

Fig. 4 shows the total and atom-resolved density of states (DOS) of ($Li_{0.8}$ $Fe_{0.2}$)OHFeSe. One notices a large number of accessible states that are widely spread into two major energy regions: between −2.75 to −6 eV and between 1.5 and −2 eV with respect to the Fermi energy (E_F). The DOS in the first energy region is mainly due to the Fe_2, Se, and O atoms. However, in the second energy region, i.e., in the energy region around the Fermi energy, the DOS is almost completely due to the Fe_1 and Fe_2 atoms. What is remarkable in this energy region is that in the direct vicinity of E_F the total DOS is dominated by the Fe_1 states. This important finding has not been observed in the total DOS of an idealized (the approximate of the real compound) compound LiOHFeSe in Ref. [23].

Whereas the electronic states due to the Fe_1 atoms are mainly located around E_F, those due to the Fe_2 atoms are spread continuously across E_F, with relatively high peaks below and above E_F (Fig. 4). There is almost no contribution to the DOS from the H atoms. However, the O and Se atoms contribute significantly to the DOS in the lower energy region, typically from −2.75 to −6 eV with respect to E_F.

The calculated DOS also provides information on the nature of chemical bonding between the different elements in the compound studied. A high degree of overlap of Fe_2, Se, and O states (Fig. 4) leads to chemical bonding of the covalent type. This confirms the conclusion derived from the calculated charge density distribution plots (*vide supra*).

The calculated electronic band structure of ($Li_{0.8}$ $Fe_{0.2}$)OHFeSe is shown in Fig. 5. One can notice a high concentration of the electronic states in the energy interval between −1.4 to 1.2 eV with respect to E_F. This is indicative of good electrical conductivity of ($Li_{0.8}$ $Fe_{0.2}$)OHFeSe. These bands are all due to the Fe atoms, as discussed earlier. One can also observe that within the Fermi energy region there is a rather small variation of a given band with energy along different symmetry directions. This points towards a small and almost constant value of the effective mass in this energy region. This results in a relatively high electron mobility, which leads to good electrical conductivity.

A high degeneracy of electronic states along the Γ direction is evident (Fig. 5), as is expected for the highest degree of symmetry in the Brillouin zone. The X and M symmetry points also show a relatively high degeneracy of electronic states. As one moves away from these high-symmetry directions, the degeneracy of electronic states is partially reduced. In other words, the electronic states remain confined to a narrow energy region and this accounts for the metallic behavior of the compound studied. A relatively dense band region is observed for low energies (below about −3 eV with respect to E_F). These states originate from the semi-core states of various atoms in ($Li_{0.8}$ $Fe_{0.2}$)OHFeSe and do not play a significant role in the electronic transport properties of this compound.

3.2.3. Hyperfine-interaction parameters

Numerical analysis of Mössbauer spectra of a non-magnetic compound yields the two most important hyperfine-interaction parameters: the isomer shift, δ_0, and the principal component of the electric field gradient (EFG) tensor, V_{zz}, with the asymmetry

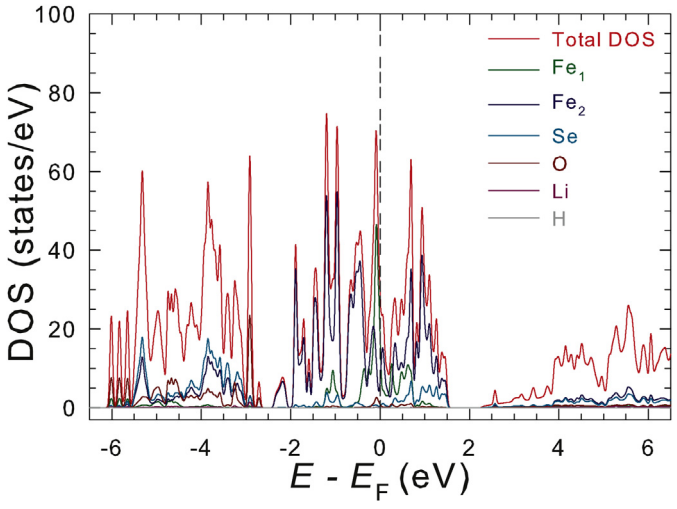

Fig. 4. Total and atom-resolved density of states of ($Li_{0.8}$ $Fe_{0.2}$)OHFeSe.

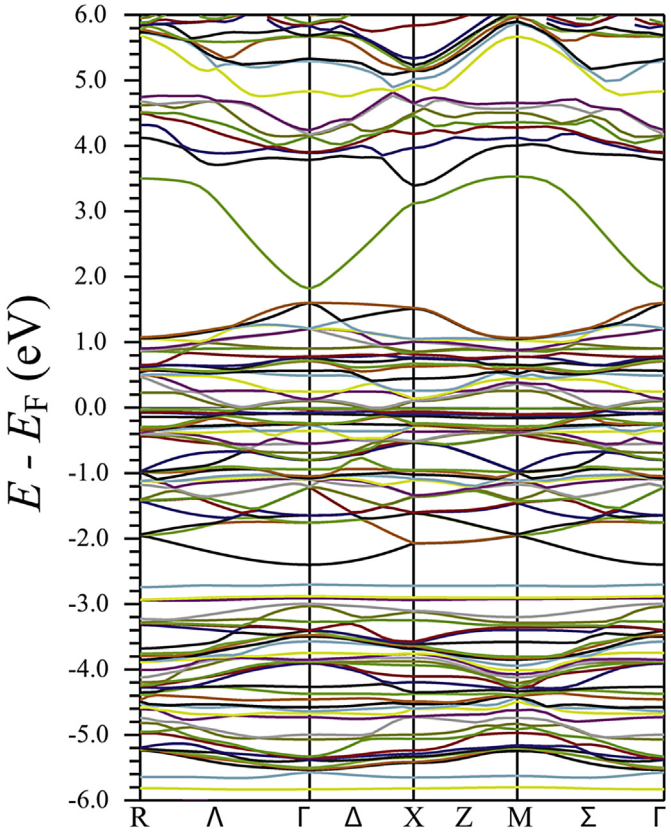

Fig. 5. Energy band structure of ($Li_{0.8}$ $Fe_{0.2}$)OHFeSe.

parameter, η [17]. If the crystal structure of a compound studied is known, these parameters in principle can be also obtained from first-principles calculations [24]. For the compound studied here, the Fe atoms are located at the sites with the point symmetry $\overline{4}$ m2 (Table 1), which ensures $\eta = 0$ at these sites.

The isomer shift results from the difference in the total electron density at the Mössbauer nucleus in the compound studied, $\rho(0)$, and in the reference compound, $\rho_{\mathrm{ref}}(0)$,

$$\delta_0 = \alpha\Big(\rho(0) - \rho_{\mathrm{ref}}(0)\Big), \tag{1}$$

where α is a calibration constant. In calculating $\rho(0)$, relativistic spin-orbit effects were invoked in order to account for the possibility of the penetration of the $p_{1/2}$ electrons into the ^{57}Fe nuclei. An α-Fe (with the *bcc* structure and the lattice constant of 2.8665 Å) was chosen as a reference compound. The calculated value of $\rho_{\mathrm{ref}}(0)$ is 15309.918 a.u.$^{-3}$. The calculated values of $\rho(0)$ at the Fe_1 and Fe_2 sites are 15307.058 and 15308.059 a.u.$^{-3}$, respectively. Using the calibration constant $\alpha = -0.291$ a.u.^{3}(mm/s) (Ref. [25]), Eq. (1) gives $\delta_{0,1} = 0.832$ mm/s and $\delta_{0,2} = 0.541$ mm/s.

The calculations of V_{zz} at the Fe_1 and Fe_2 sites yielded the values of -6.762×10^{21} and 0.505×10^{21} V/m^2, respectively. The quadrupole splitting (the distance between two resonance lines in a quadrupole doublet) is defined [17] as $\Delta = \frac{1}{2}eQ\left|V_{zz}\right|$, where e is the proton charge and Q is the electric quadrupole moment of the ^{57}Fe nucleus [26]. Thus, the calculated values of V_{zz} at the Fe_1 and Fe_2 sites correspond to $\Delta_1 = 1.055$ mm/s and $\Delta_2 = 0.079$ mm/s, respectively.

The above calculations thus predict that the quadrupole doublet due to Fe atoms at the Fe_1 site should have larger δ_0 and Δ values than the values corresponding to the quadrupole doublet due to Fe atoms at the Fe_2 site.

3.3. Mössbauer spectroscopy

We measured first ^{57}Fe Mössbauer spectra of $(Li_{0.8}\ Fe_{0.2})$OHFeSe over a large velocity range (Figs. 6 and 7) in order to identify possible patterns originating from a magnetic/nonmagnetic impurity phase. Down to ~77 K (Fig. 6), in addition to two quadrupole doublets due to Fe atoms at the Fe_1 and Fe_2 sites (Table 1) of the main phase, one clearly observes a quadrupole doublet originating from the nonmagnetic impurity phase (the asymmetry of the more intense Fe_2 quadrupole doublet is caused by preferred orientation

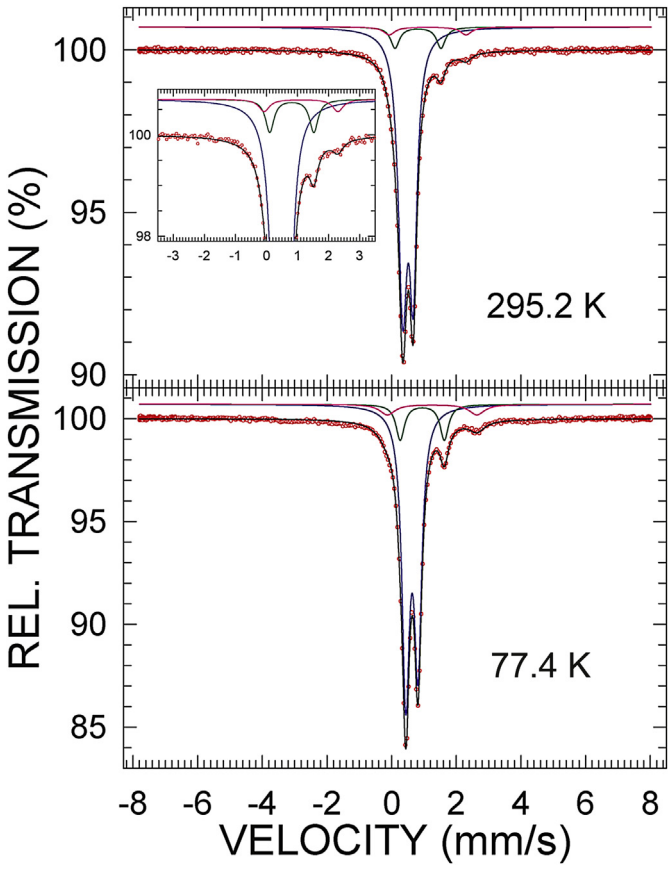

Fig. 6. ^{57}Fe Mössbauer spectra of $(Li_{0.8}\ Fe_{0.2})$OHFeSe at the indicated temperatures fitted (black solid lines) with two quadrupole doublets (blue and dark green solid lines) due to Fe_2 and Fe_1 atoms (Table 1) of the main phase, and a quadrupole doublet (pink solid lines) originating from the impurity phase. The inset shows the 295.2 K spectrum with enlarged vertical and horizontal scales. The zero-velocity origin is relative to α-Fe at room temperature. (For interpretation of the references to colour in this figure legend, the reader is referred to the web version of this article.)

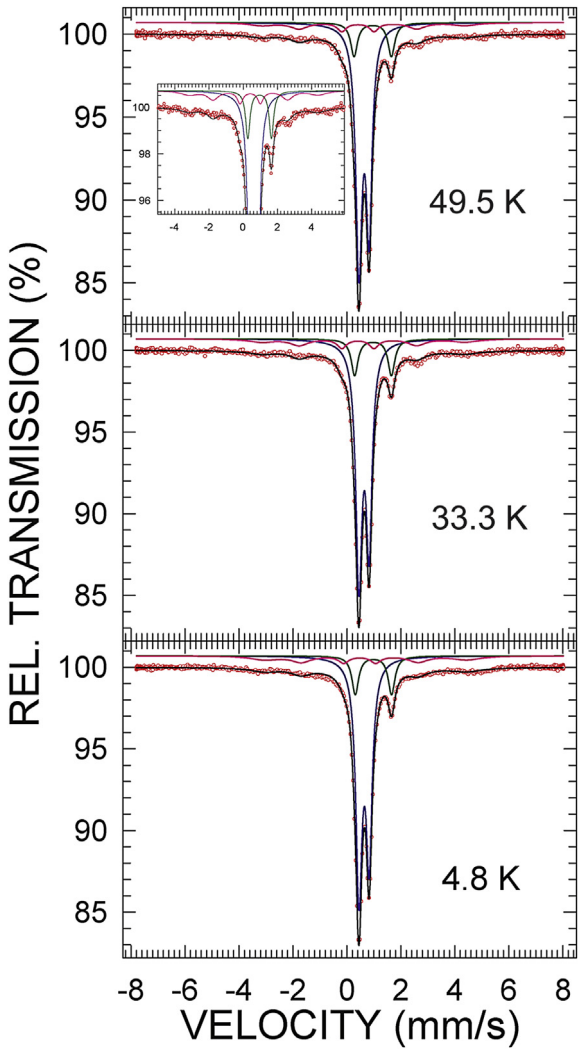

Fig. 7. ^{57}Fe Mössbauer spectra of $(Li_{0.8}\ Fe_{0.2})$OHFeSe at the indicated temperatures fitted (black solid lines) with two quadrupole doublets (blue and dark green solid lines) due to Fe_2 and Fe_1 atoms (Table 1) of the main phase, and a Zeeman pattern (pink solid lines) originating from the impurity phase. The inset shows the 49.5 K spectrum with enlarged vertical and horizontal scales. The zero-velocity origin is relative to α-Fe at room temperature. (For interpretation of the references to colour in this figure legend, the reader is referred to the web version of this article.)

(texture) in the polycrystalline Mössbauer absorber; this asymmetry cannot be detected in the less intense Fe_1 and impurity-phase doublets). Below ~50 K (Fig. 7), the two quadrupole doublets due to Fe atoms at the Fe_1 and Fe_2 sites persist, and the impurity phase becomes magnetically ordered and consequently its Mössbauer spectrum is in the form of a Zeeman pattern. It is thus clear that the ordering temperature of the impurity phase is between 50 and 77 K. The fact that the two quadrupole doublets due to Fe atoms at the Fe_1 and Fe_2 sites persist down to 4.8 K (Fig. 7) already indicates the absence of any magnetic order of the Fe_1- and Fe_2-site Fe atoms down to 4.8 K.

To verify this preliminary conclusion, and to obtain precise hyperfine-interaction parameters of the Fe_1- and Fe_2-site Mössbauer patterns, Mössbauer measurements were carried out over a small velocity range at various temperatures down to 2.0 K (Figs. 8 and 9). It is clear that the Mössbauer pattern originating from the impurity phase is in the form of a quadrupole doublet (Zeeman pattern) for temperatures above (below) ~78 K. The presence of two quadrupole doublets due to Fe atoms at the Fe_1 and Fe_2 sites (Table 1) down to 2.0 K, i.e., the absence of any sign of Zeeman patterns originating from these two sites, proves unambiguously that there is no magnetic order of the Fe magnetic moments in the 40 K superconductor $(Li_{0.8}\ Fe_{0.2})$OHFeSe down to 2.0 K.

^{57}Fe Mössbauer spectra of the 43 K superconductor $(Li_{0.8}\ Fe_{0.2})$ $OH(Fe_{0.92}\ Li)0.08$ Se at 30 and 2.1 K are presented in Ref. [13]. The observed broadening of the 2.1 K spectrum as compared to that of the 30 K spectrum was accounted for by a Zeeman pattern originating from the Fe atoms at the Fe_1 site with the hyperfine magnetic field $H_{hf} = 30$ kOe [13]. The presence of this Zeeman pattern was taken as evidence [13] for the coexistence of 3*d* ferromagnetism associated with the Fe_1-site Fe atoms and superconductivity. Fig. 10 shows a comparison between the Fe_1-site component of the 2.0 K spectrum in the form of a quadrupole doublet (Fig. 9) and the corresponding component in the form of a Zeeman pattern with $H_{hf} = 30$ kOe. The presence of the latter component should be reflected in a distinct absorption in the experimental spectrum at the velocity of ~2.1 mm/s. Since such a distinct absorption is not observed in the 2.0 K experimental spectrum (Fig. 10), it is suggested that the broadening of the 2.1 K spectrum observed in Ref. 13 is of extrinsic origin.

The fits of the Mössbauer spectra in Figs. 8 and 9 with two Fe_1- and Fe_2-site quadrupole-doublet components yield the following

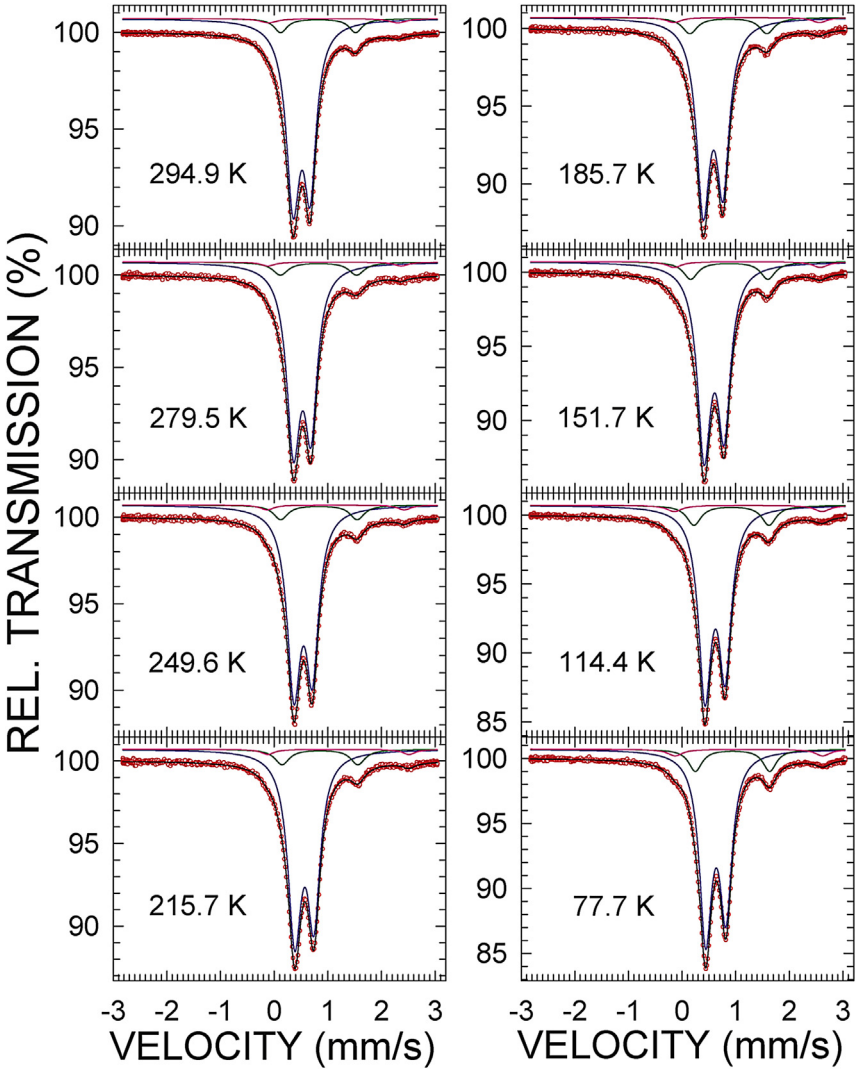

Fig. 8. ^{57}Fe Mössbauer spectra of $(Li_{0.8}\ Fe_{0.2})$OHFeSe at the indicated temperatures fitted (black solid lines) with two quadrupole doublets (blue and dark green solid lines) due to Fe_2 and Fe_1 atoms (Table 1) of the main phase, and a quadrupole doublet (pink solid lines) originating from the impurity phase. The zero-velocity origin is relative to α-Fe at room temperature. (For interpretation of the references to colour in this figure legend, the reader is referred to the web version of this article.)

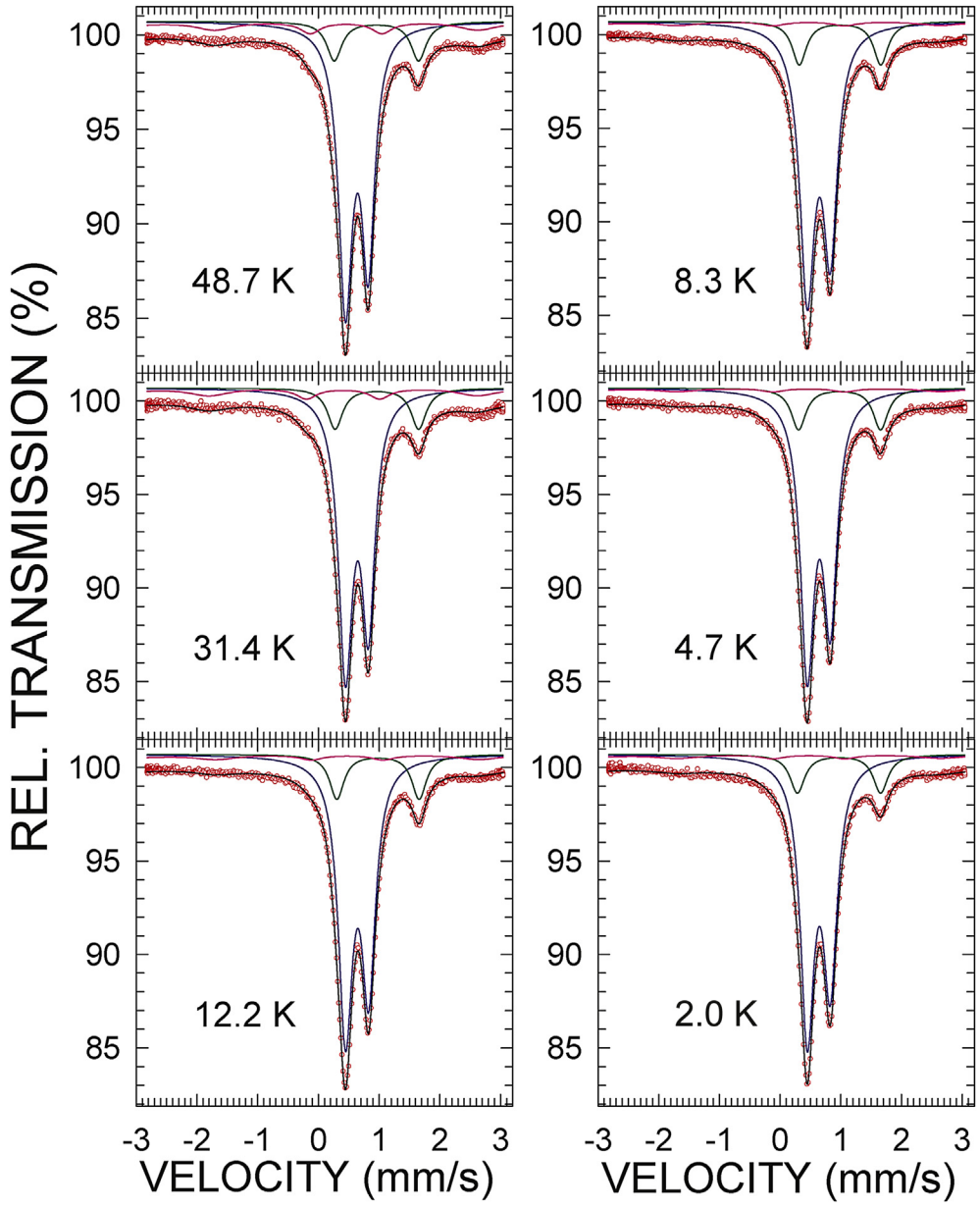

Fig. 9. ^{57}Fe Mössbauer spectra of ($Li_{0.8}$ $Fe_{0.2}$)OHFeSe at the indicated temperatures fitted (black solid lines) with two quadrupole doublets (blue and dark green solid lines) due to Fe_2 and Fe_1 atoms (Table 1) of the main phase, and a Zeeman pattern (pink solid lines) originating from the impurity phase. The zero-velocity origin is relative to α-Fe at room temperature. (For interpretation of the references to colour in this figure legend, the reader is referred to the web version of this article.)

parameters: the quadrupole splitting Δ, the absorber linewidth Γ, and the centre shift δ (relative to α-Fe at 298 K) [17].

Fig. 11 shows the temperature dependence of Δ_i and Γ_i (i = 1,2). The values of Δ_1 and Δ_2 at 0 K, obtained from the extrapolation of the low-temperature data, are 1.351(12) and 0.380(1) mm/s, respectively. They are higher than the corresponding calculated values of 1.055 and 0.079 mm/s. One observes that Δ_1 is approximately constant at temperatures above ~150 K and then decreases at lower temperatures, whereas Δ_2 is approximately constant at temperatures below ~150 K and then decreases at higher temperatures. A sudden decrease(increase) of $\Delta_1(\Delta_2)$ below(above) ~150 K could be, in principle, caused by a possible structural phase transition at ~150 K. However, there is no evidence for such a structural transition in the neutron diffraction data [11]. The observed temperature dependence of Δ_1 and Δ_2 must be the result of crystal-field effects [27] on the electronic states of ferrous ions (for ferric ions, Δ is nearly invariant with temperature) [17]. The absorber linewidths Γ_1 and Γ_2 (Fig. 11) change very little with temperature. In particular, there is no sign of a dramatic increase of Γ_1 at low temperatures, as observed in Ref. 13, that might indicate magnetic ordering of the Fe_1-site Fe atoms at ~8.5 K.

The temperature dependence of $\delta_i(T)$ (i = 1,2) is shown in Fig. 12. In general, $\delta(T)$ consists of two contributions

$$\delta(T) = \delta_0 + \delta_{SOD}(T), \quad (2)$$

where δ_0 is the intrinsic, temperature-independent isomer shift and $\delta_{SOD}(T)$ is the second-order Doppler (SOD) shift which depends on the lattice vibrations of the Fe atoms [17]. The latter contribution varies significantly with temperature and can be expressed in terms of the Debye approximation of the lattice vibrations as

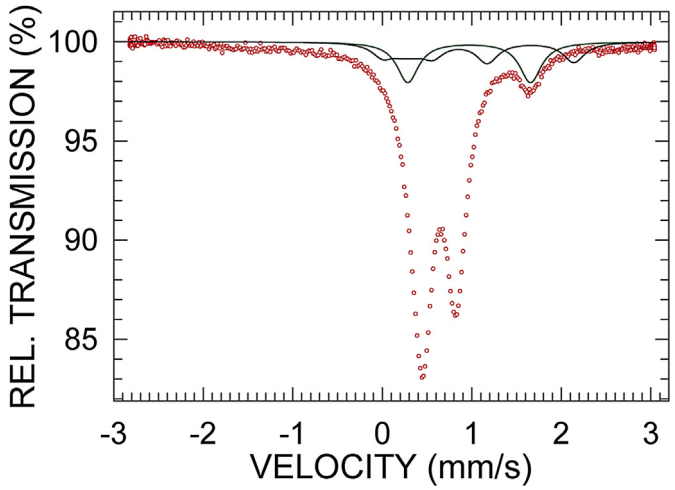

Fig. 10. ^{57}Fe Mössbauer spectrum of ($Li_{0.8}$ $Fe_{0.2}$)OHFeSe at 2.0 K. The contribution of the Fe_1 atoms in the form of a quadrupole doublet (dark green line) is compared with the corresponding contribution in the form of a Zeeman pattern with H_{hf} = 30 kOe from Ref. [13]. The zero-velocity origin is relative to α-Fe at room temperature. (For interpretation of the references to colour in this figure legend, the reader is referred to the web version of this article.)

$$\delta_{SOD}(T) = -\frac{9}{2}\frac{k_B T}{Mc}\left(\frac{T}{\Theta_D}\right)^3 \int_0^{\Theta_D/T} \frac{x^3 dx}{e^x - 1}, \quad (3)$$

where k_B is the Boltzmann constant, M is the mass of the Mössbauer nucleus, c is the speed of light, and Θ_D is the Debye temperature. By fitting the experimental data $\delta_i(T)$ (Fig. 12) to Eq. (2), the quantities $\delta_{0,i}$ and $\Theta_{D,i}$ were found to be $\delta_{0,1} = 0.974(5)$ mm/s, $\Theta_{D,1} = 186(21)$ K, and $\delta_{0,2} = 0.636(1)$ mm/s, $\Theta_{D,2} = 397(4)$ K. The experimental values of $\delta_{0,1}$ and $\delta_{0,2}$ are close to the corresponding calculated values of 0.832 and 0.541 mm/s. The observed inequality $\Theta_{D,1} < \Theta_{D,2}$ is indicative of a much larger bonding strength of the Fe atoms at the Fe_2 sites than at the Fe_1 sites. We note here that the experimental values of $\delta_{0,i}$ and Δ_i (i = 1,2) fulfill the theoretically predicted inequalities $\delta_{0,1} > \delta_{0,2}$ and $\Delta_1 > \Delta_2$.

Knowledge of Θ_D at a given crystallographic site allows one to calculate the absorber Debye-Waller factor f_a at any temperature T at that site from the expression

$$f_a(T) = \exp\left\{-\frac{3}{4}\frac{E_\gamma^2}{Mc^2 k_B \Theta_D}\left[1 + 4\left(\frac{T}{\Theta_D}\right)^2 \int_0^{\Theta_D/T} \frac{x dx}{e^x - 1}\right]\right\}, \quad (4)$$

where E_γ is the energy of the Mössbauer transition [17]. As the absorption spectral area A of a component Mössbauer pattern due to Fe atoms at a given site, that is determined from the transmission integral fit [19], is proportional to the product of the concentration of Fe, N, and f_a at that site, the absorption spectral area ratio of the Fe_1- and Fe_2-site quadrupole doublets is

$$\frac{A_1(T)}{A_2(T)} = \frac{N_1 f_{a,1}(T)}{N_2 f_{a,2}(T)}. \quad (5)$$

The fit of the 2.0 K Mössbauer spectrum (Fig. 9) yields $\frac{A_1}{A_2} = 0.1642(54)$. The values of $f_{a,1}$ and $f_{a,2}$ at 2.0 K are calculated from Eq. (4). This leads [(Eq. (5)] to $\frac{N_1}{N_2} = 0.181(6)$. This value of $\frac{N_1}{N_2}$ is in excellent agreement with the value of 0.18(1) (Table 1) determined from Rietveld analysis.

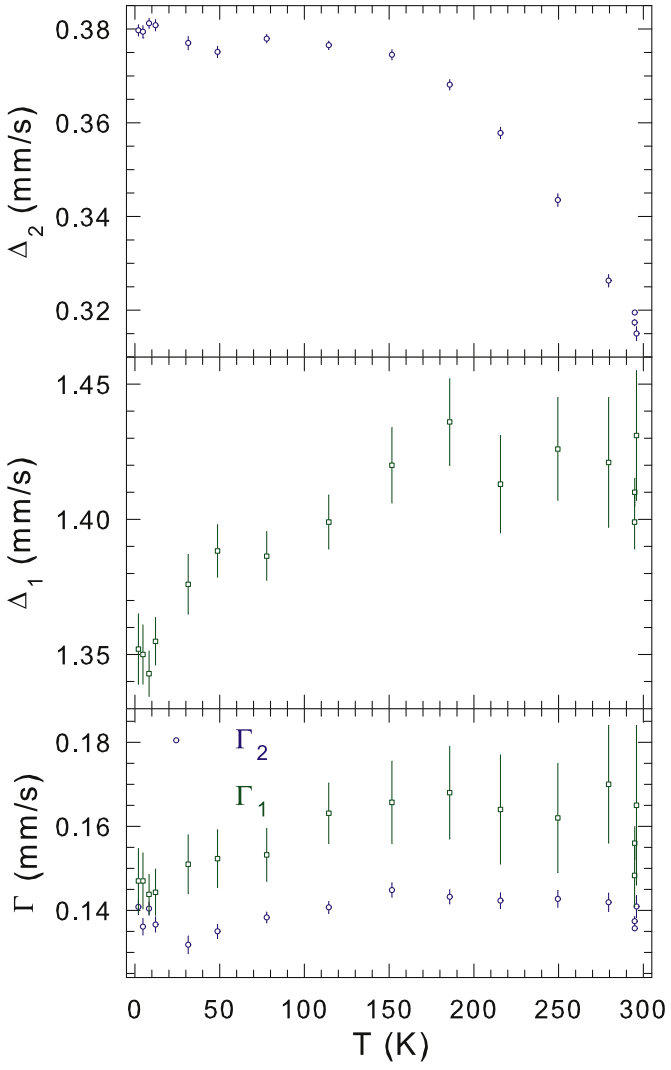

Fig. 11. Temperature dependence of the quadrupole splitting Δ of Fe at the Fe_2 and Fe_1 sites (Table 1) and of the corresponding absorber linewidth Γ.

4. Summary

The results of x-ray diffraction and ^{57}Fe Mössbauer spectroscopy measurements, complemented by *ab-initio* electronic structure and the hyperfine-interaction parameters calculations, of the recently discovered 40 K superconductor ($Li_{0.8}$ $Fe_{0.2}$)OHFeSe are presented. The superconductor studied is shown to crystallize in the tetragonal space group *P*4/*nmm* with the lattice constants $a = 3.7865(2)$ Å and $c = 9.2802(6)$ Å. It exhibits a mixture of strong covalent and weak ionic chemical bonding and has metallic characteristics. The Mössbauer spectra measured in the temperature range 2.0–294.9 K are the superposition of two quadrupole-doublet components originating from Fe atoms located at the 2*a* and 2*b* sites. We prove that, despite recent claims to the contrary, there is no magnetic ordering of the 2*a*-site Fe magnetic moments down to 2.0 K. General agreement between the calculated hyperfine-interaction parameters at the two Fe sites and the experimental ones is observed. We find that the Debye temperatures for the 2*a* and 2*b* sites are 186(21) and 397(4) K, respectively. The Fe concentration ratio at the 2*a* and 2*b* sites determined from Rietveld analysis is in excellent agreement with that derived from Mössbauer spectroscopy.

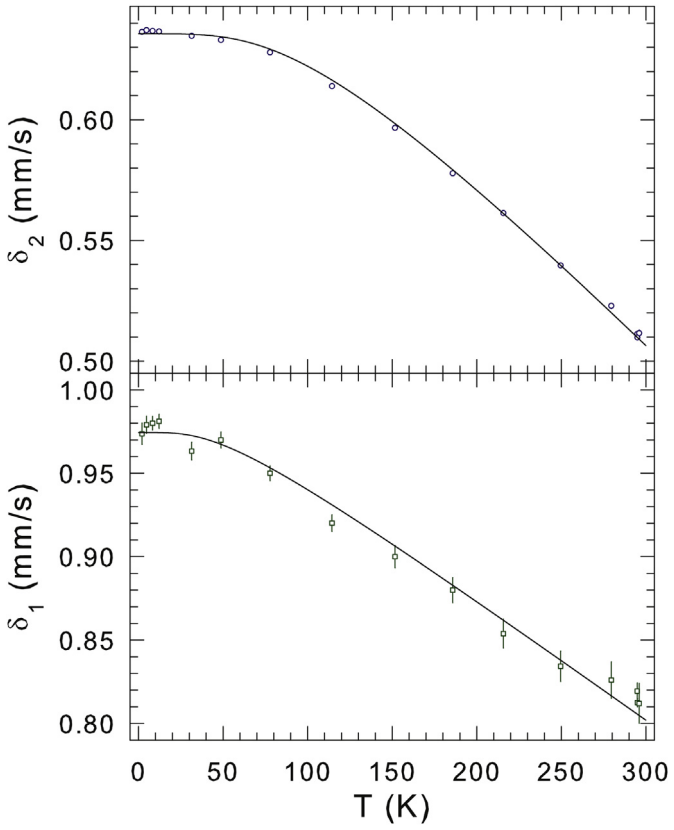

Fig. 12. Temperature dependence of the centre shift δ of the Fe_2- and Fe_1-site quadrupole doublets. The solid lines are the fits to Eq. (1), as explained in the text.

Acknowledgments

This work was supported by the Natural Sciences and Engineering Research Council of Canada. We thank X. F. Lu and X. H. Chen for providing the sample of $(Li_{0.8}\ Fe_{0.2})$OHFeSe.

References

[1] F.C. Hsu, J.Y. Luo, K.W. Yeh, T.K. Chen, T.W. Huang, P.M. Wu, Y.C. Lee, Y.L. Huang, Y.Y. Chu, D.C. Yan, M.K. Wu, Proc. Natl. Acad. Sci. 105 (2008) 14262.
[2] T.M. McQueen, Q. Huang, V. Ksenofontov, C. Felser, Q. Xu, H. Zandbergen, Y.S. Hor, J. Allred, A.J. Williams, D. Qu, J. Checkelsky, N.P. Ong, R.J. Cava, Phys. Rev. B 79 (2009) 014522.
[3] T.P. Ying, X.L. Chen, G. Wang, S.F. Jin, T.T. Zhou, X.F. Lai, H. Zhang, W.Y. Wang, Sci. Rep. 2 (2012) 426.
[4] E. Dagotto, Rev. Mod. Phys. 85 (2013) 849 (and references therein).
[5] A. Krzton-Maziopa, E.V. Pomjakushina, V. Yu. Pomjakushin, F. von Rohr, A. Schilling, K. Conder, J. Phys. Condens. Matter 24 (2012) 382202.
[6] M. Burrard-Lucas, D.G. Free, S.J. Sedlmaier, J.D. Wright, S.J. Cassidy, Y. Hara, A.J. Corkett, T. Lancaster, P.J. Baker, S.J. Blundell, S.J. Clarke, Nat. Mater 12 (2013) 15.
[7] Q.Y. Wang, Z. Li, W.H. Zhang, Z.C. Zhang, J.S. Zhang, W. Li, H. Ding, Y.B. Ou, P. Deng, K. Chang, J. Wen, C.L. Song, K. He, J.F. Jia, S.H. Ji, Y.Y. Wang, L.L. Wang, X. Chen, X.C. Ma, Q.K. Xue, Chin. Phys. Lett. 29 (2012) 037402.
[8] D. Liu, W. Zhang, D. Mou, J. He, Y.B. Ou, Q.Y. Wang, Z. Li, L. Wang, L. Zhao, S. He, Y. Peng, X. Liu, C. Chen, L. Yu, G. Liu, X. Dong, J. Zhang, C. Chen, Z. Xu, J. Hu, X. Chen, X. Ma, Q. Xue, X.J. Zhou, Nat. Commun. 3 (2012) 931.
[9] S. He, J. He, W. Zhang, L. Zhao, D. Liu, X. Liu, D. Mou, Y.B. Ou, Q.Y. Wang, Z. Li, L. Wang, Y. Peng, Y. Liu, C. Chen, L. Yu, G. Liu, X. Dong, J. Zhang, C. Chen, Z. Xu, X. Chen, X. Ma, Q. Xue, X.J. Zhou, Nat. Mater 12 (2013) 605.
[10] S. Tan, Y. Zhang, M. Xia, Z. Ye, F. Chen, X. Xie, R. Peng, D. Xu, Q. Fan, H. Xu, J. Jiang, T. Zhang, X. Lai, T. Xiang, J. Hu, B. Xie, D. Feng, Nat. Mater 12 (2013) 634.
[11] X.F. Lu, N.Z. Wang, H. Wu, Y.P. Wu, D. Zhao, X.Z. Zeng, X.G. Luo, T. Wu, W. Bao, G.H. Zhang, F.Q. Huang, X.H. Chen, Nat. Mater 14 (2015) 325.
[12] Y.P. Wu, D. Zhao, X.R. Lian, X.F. Lu, N.Z. Wang, X.G. Luo, X.H. Chen, T. Wu, Phys. Rev. B 91 (2015) 125107.
[13] U. Pachmayr, F. Nitsche, H. Luetkens, S. Kamusella, F. Brückner, R. Sarkar, H.-H. Klauss, D. Johrendt, Angew. Chem. Int. Ed. 54 (2015) 293.
[14] X. Dong, H. Zhou, H. Yang, J. Yuan, K. Jin, F. Zhou, D. Yuan, L. Wei, J. Li, X. Wang, G. Zhang, Z. Zhao, J. Am. Chem. Soc. 137 (2015) 66.
[15] H. Sun, D.N. Woodruff, S.J. Cassidy, G.M. Allcroft, S.J. Sedlmaier, A.L. Thompson, P.A. Bingham, S.D. Forder, S. Cartenet, N. Mary, S. Ramos, F.R. Foronda, B.H. Williams, X. Li, S.J. Blundell, S.J. Clarke, Inorg. Chem. 54 (2015) 1958.
[16] U. Pachmayr, D. Johrendt, Chem. Commun. 51 (2015) 4689.
[17] N.N. Greenwood, T.C. Gibb, Mössbauer Spectroscopy, Chapman and Hall, London, 1971. P. Gütlich, E. Bill, and A. Trautwein, Mössbauer Spectroscopy and Transition Metal Chemistry (Springer, Berlin, 2011).
[18] Certificate of Calibration, in: J.P. Cali (Ed.), Iron Foil Mössbauer Standard, Natl. Bur. Stand. (U.S.) Circ. No. 1541, GPO, U.S., 1971. Washington, D.C.
[19] S. Margulies, J.R. Ehrman, Nucl. Instrum. Methods 12 (1961) 131. G. K. Shenoy, J. M. Friedt, H. Maletta, and S. L. Ruby, in Mössbauer Effect Methodology, edited by I. J. Gruverman, C. W. Seidel, and D. K. Dieterly (Plenum, New York, 1974), Vol. 10, p. 277.
[20] P. Blaha, K. Schwartz, G. Madsen, D. Kvasnicka, J. Luitz, WIEN2k, an Augmented Plane Wave Plus Local Orbitals Program for Calculating Crystal Properties, Karlheinz Schwarz, Technical Universität Wien, Austria, 1999.
[21] J.P. Perdew, S. Burke, M. Ernzerhof, Phys. Rev. Lett. 77 (1996) 3865.
[22] R.A. Young, The Rietveld Method, Oxford University Press, Oxford, 1993.
[23] I.A. Nekrasov, M.V. Sadovskii, JETP Lett. 101 (2015) 47.
[24] P. Blaha, J. Phys. Conf. Ser. 217 (2010) 012009.
[25] U.D. Wdowik, K. Reubenbauer, Phys. Rev. B 76 (2007) 155118.
[26] G. Martínez-Pinedo, P. Schwerdtfeger, E. Caurier, K. Langanke, W. Nazarewich, T. Söhnel, Phys. Rev. Lett. 87 (2001) 062701.
[27] R. Ingalls, Phys. Rev. 133 (1964) A787.